catalysts

MDPI

Article

In Situ SERS Monitoring of Schiff Base Reactions via Nanoparticles on a Mirror Platform

Binbin Chen [1,2,†], Shiyong Meng [1,2,†], Danmin Liu [1], Qingsong Deng [1,*] and Cong Wang [1,*]

[1] Beijing Key Laboratory of Microstructure and Property of Advanced Materials, College of Materials Science and Engineering, Beijing University of Technology, Beijing 100124, China; binbinchen@emails.bjut.edu.cn (B.C.); s202377069@emails.bjut.edu.cn (S.M.)
[2] College of Physics and Optoelectronic Engineering, Beijing University of Technology, Beijing 100124, China
* Correspondence: qsdeng@bjut.edu.cn (Q.D.); smartswang@bjut.edu.cn (C.W.)
† These authors contributed equally to this work.

Abstract: Schiff base reactions are widely used in pharmacy, catalysis, and volatile aldehyde detection. However, common biomarker sensing methods struggle to monitor this reaction process precisely due to their sensitivity, their time-consuming nature, and complex substrates. Here, we introduce the Nanoparticle-on-Mirror structure for in situ monitoring this reaction process through the application of a Au nanoparticle-p-Aminothiophenol-Au thin-film platform by surface-enhanced Raman scattering (SERS). Owing to the exposure of -NH_2 groups and the local ultra-strong electromagnetic field in the nanocavity, the Schiff base reactions process can be rapidly monitored within two minutes. Meanwhile, the monitoring platform can detect benzaldehyde molecules as low as 10^{-6} M, showing excellent SERS performance. Notably, the Au-nanoparticle-p-Aminothiophenol-Au thin-film platform exhibited anti-interference and specificity, being able to identify BA in the presence of interference. The use of the Au-nanoparticle-p-Aminothiophenol-Au thin-film platform provides a sensing method for Schiff base reactions with accuracy and simplicity of operation, achieving a balanced approach for low-cost and high-performance real-time monitoring, which is expected to be applied in various catalytic reaction process monitoring and catalyst design processes.

Keywords: surface-enhanced Raman scattering; in situ monitoring; Au nanoparticle-p-Aminothiophenol-Au thin film; Schiff base; anti-interference

check for updates

Citation: Chen, B.; Meng, S.; Liu, D.; Deng, Q.; Wang, C. In Situ SERS Monitoring of Schiff Base Reactions via Nanoparticles on a Mirror Platform. *Catalysts* **2024**, *14*, 803. https://doi.org/10.3390/catal14110803

Academic Editor: Aleksander Filarowski

Received: 30 September 2024
Revised: 30 October 2024
Accepted: 4 November 2024
Published: 8 November 2024

Copyright: © 2024 by the authors. Licensee MDPI, Basel, Switzerland. This article is an open access article distributed under the terms and conditions of the Creative Commons Attribution (CC BY) license (https://creativecommons.org/licenses/by/4.0/).

1. Introduction

Surface-enhanced Raman scattering (SERS) is a highly sensitive and selective spectral analysis technique, which can greatly enhance the Raman scattering signal, making it possible to detect and analyze trace samples [1–4]. The SERS effect mainly relies on two mechanisms: electromagnetic enhancement and chemical enhancement. The electromagnetic enhancement results from the surface plasmon resonance on the surface of metal nanostructures, which is formed by collective oscillations initiated by the mutual coupling of free electrons and photons at the metal surface [5]. It can significantly increase the strength of the local electromagnetic field, thus greatly enhancing the Raman scattered signal [6,7]. The emergence of SERS technology has brought a revolutionary change to the field of chemical reaction monitoring. It can not only monitor the progress of chemical reactions in real time but also provide detailed information on molecular structure changes during the reaction process, providing a powerful tool for gaining an in-depth understanding of the chemical reaction mechanism. The chemical enhancement is related to the chemical interaction between the molecule and the metal surface, which can further improve the efficiency of Raman scattering. Through carefully designed metal nanostructures, such as Au, Ag and Cu nanoparticles or nanoislands, efficient SERS substrates can be constructed to achieve the high-sensitivity monitoring of chemical reactions [8].

In chemical reaction monitoring, SERS technology can track the consumption of reactants, the generation of products, and the presence of intermediates in real time, which is crucial for understanding reaction kinetics and reaction mechanisms. For example, in the chemical reaction on the catalyst surface, the interaction between the reactants and the catalyst surface and the changes in surface species during the reaction can be observed through SERS, which helps to reveal the active site and reaction path of the catalyst. In addition, SERS can be used to monitor the behavior of biomolecules in chemical reactions, providing important information for drug discovery and biocatalytic process.

The Nanoparticle-on-Mirror (NPoM) structure has a unique application value when using SERS technology [9], and it can be simply prepared by placing nanoparticles (NPs) on a flat metallic mirror (film) [10]. It is an efficient SERS substrate design with NPs that can significantly enhance Raman signals to achieve the high-sensitivity detection of chemical substances. As early as 2005, Kim et al. studied the Raman scattering signals of a p-Aminothiophenol (PATP) monolayer assembled on a macroscopic smooth Au film and attributed their unique enhancement signal to the electromagnetic coupling of the localized surface plasmon derived from Ag (Au) NPs to the surface plasmon of the underlying Au thin film [11]. Since then, similar structures have been extensively studied. In 2010, Park et al. observed the fluctuations of single-molecule Raman signals by constructing Au nanoparticle-molecule-Au thin-film junctions, which can yield strong local electromagnetic fields in the narrow metallic gap [12]. In 2016, Chikkaraddy et al. observed strong coupling behavior between a single molecule and a nanocavity at room temperature by designing a nanocavity so that its gap plasmon frequency matches that of the molecule [13]. In summary, NPoM structures are of wide research and application value because of the small volume and stronger field enhancement that can occur in the subnanoscale gaps between their paired plasmons nanoparticles [14]. In addition, the NPoM structure is easy to prepare, has a relatively low cost, and has good reproducibility, which makes it have a wide range of applications in chemical analysis, biological detection, and environmental monitoring [15,16].

Volatile organic compounds (VOCs) are very important warning signs in food analysis, medical diagnosis, environmental pollution, etc. Schiff base reactions are often used to monitor volatile aldehydes [17]. Compared with the standard gas detection techniques such as chromatography and mass spectrometry, SERS sensors has the advantages of simple operation and sample preparation, fast analysis speed, and high sensitivity [18]. However, aldehydes usually have a low Raman scattering cross-section and are not adsorbent on the surfaces of metals, so the usual SERS strategy is mainly to concentrate and capture aldehydes through the Schiff base reactions of the probe [19]. In addition, miniaturized gas film separation arrays and microfluidic systems are used to increase the probability of collisions between gas molecules and sensors to further eliminate interference from matrix signals [20–22]. Obviously, the above methods need to prepare complex SERS substrates, which is not conducive to conducting various exploratory experiments. More importantly, such structures are applied to explore the mechanism of the plasmonic catalyst. Huh and co-workers utilized NPoM systems to explore how plasmon excitation leads to the C-C bond cleavage of the molecules in the nanogap, which can be observed by SERS spectra [23]. Gao and co-workers designed Au NP/NiO/Au film plasmonic photocatalysts to enhance internal quantum efficiency by 14 times compared to a similar system without a coupling effect [24]. Therefore, the NPoM structure not only can serve as a ultrasensitive sensor but also holds significant potential for revealing the principles of plasmonic catalysis.

In this work, NPoM was used as a chemical reaction detection platform. The PATP monolayer self-assembled on the Au film served as the probe molecule, and then the uniformly sized Au NPs were spin-coated onto the substrate, resulting in the formation of a Au nanoparticle-PATP-Au thin film (NP-PATP-Au TF) structure. The real-time detection of the chemical reaction was realized by directly dropping ethanol solution of benzaldehyde (BA) molecules onto the prepared NP-PATP-TF chip. Subsequently, the platform's limit of low detection for BA was confirmed, providing a certain potential for practical applications.

We attribute this to the exposure of the -NH_2 functional group of the PATP molecule and the non-specific field enhancement in the nanocavity, which imply the potential for the NPoM chemical reaction monitoring platform to be extended to the detection of catalytic reactions at the single-atom level [25].

2. Results and Discussion

2.1. In Situ SERS Monitoring Schiff Base Reactions

Figure 1A shows images of the NP-PATP-Au TF chip under a scanning electron microscope (SEM), while Figure 1B shows the elemental mapping image of sulfur on Au TF that is uniformly detected, indicating the successful assembly of the PATP monolayer. In order to conduct a comparative study systematically, the SEM image of Au NP_S on silicon wafer and the corresponding elemental mapping image of sulfur can be seen in Figure 1C,D. Sulfur is almost undetectable on Au TF, where there is no PATP monolayer, as shown in Figure 1D. Figure S1 provides cross-sectional SEM images of the chip, confirming that the Au film on the silicon wafer is at the hundreds of nanometer scale. It can be seen that the distribution of the Au NPs is relatively uniform, and there is no secondary structure, revealing that our preparation method provides the necessary conditions for obtaining good repeatability in the Raman test. The Au-S bond formed by PATP on the Au film can be proved by the Raman spectra and X-ray photoelectron spectroscopy XPS spectra of Au. By changing the adsorption substrate, Figure S2 clearly identifies the characteristic peak of Au-S at 267 cm^{-1}, while the characteristic peak of -SH at about 2600 cm^{-1} does not exist [26]. At the same time, the binding energy of Au before and after bonding changes greatly, as depicted in Figure S3. The before and after binding energies of the Au film are about 87.92 eV and 84.25 eV. After bonding, the binding energy of Au moves to the right by about 0.88 eV and the binding energy of Au shifts to the left, suggesting that Au transfers considerable electrons to PATP through the Au-S bond.

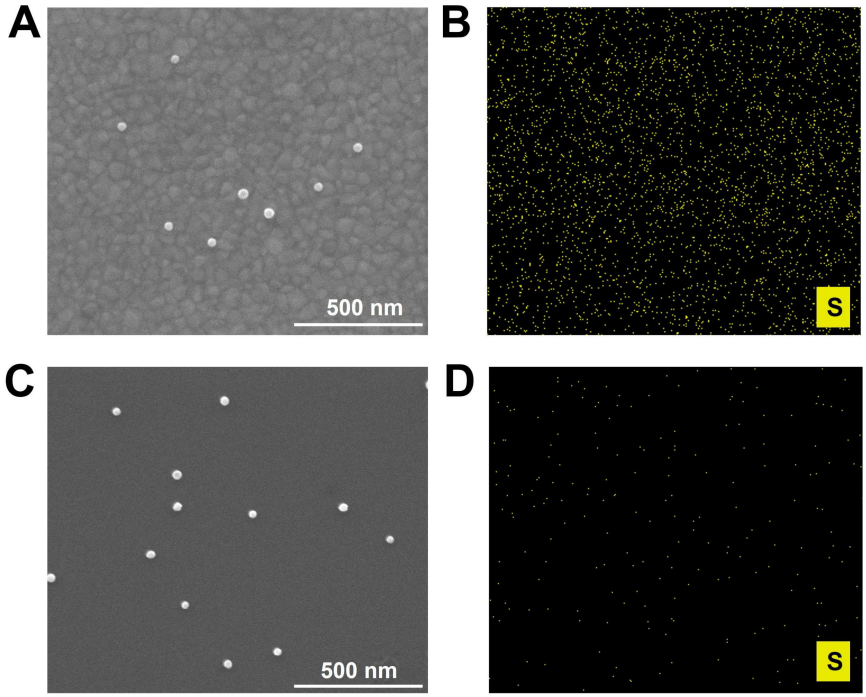

Figure 1. (**A**) An SEM image of NP-PATP-Au TF and (**B**) an elemental mapping image of the sulfur of the corresponding area. (**C**) An SEM image of Au NP_S on silicon wafer and (**D**) an elemental mapping image of the sulfur of the corresponding area.

The sensing mechanism is depicted in Figure 2A. Liquid BA was dropped onto a Au TF and interacted with the -NH_2 group of PATP modified on an Au TF to form a

Schiff base complex. Figure 2B shows the time-dependent SERS spectrum immediately after the addition of BA (10^{-3} M) under continuous 785 nm laser irradiation. As can be seen from the figure, the Raman spectrum of NP-PATP-TF did not change significantly under continuous laser irradiation, indicating that the molecules were not or only slightly damaged by light. After the BA solution was added at 30 s, the baseline of the global Raman signal rapidly increased, mainly because the presence of ethanol solution enhanced the overall fluorescence background signal. It can be seen in Figure 2B that after the decrease in BA, a new peak appears in the Raman spectrum at 1620 cm^{-1}, which is attributed to the vibration peak of the C=N group of the Schiff base [27], and the peak strength of the peak is stable at around 100 s, indicating that the reaction has almost ended at this time, because the reaction needs to be carried out in the liquid phase process, and the liquid phase environment gradually disappears with the extension of time. Figure 2C shows a local magnification of Figure 2B, which enables a more intuitive observation of the C=N feature at 1620 cm^{-1}. Figure 2D shows SERS spectra at different times before and after the reaction. Before BA solution is added, the spectral line shown reflects the characteristic peak curve of PATP, and it is very smooth at 1620 cm^{-1}. When BA is added, the peak at 1620 cm^{-1} appears almost immediately, and this surface reaction occurs very rapidly in the nanocavities designed. At the same time, the vibration of the C-H stretching peak (b_2 mode) at 1142 cm^{-1} is more obvious [11], which shows that electrons are transferred through the benzene ring, thus affecting the asymmetric vibration peak sensitive to electron transfer on the benzene ring. The vibration peak modes of PATP are shown in Table S1. In addition, the characteristic peak corresponding to benzoic acid at 885 cm^{-1} appears after drip addition and gradually weakens with the reaction, but when the Schiff base reaction is terminated, the peak is still obvious, which indicates that the benzaldehyde added to the system is excessive. Because the density of PATP on Au film is 3.3 molecules/nm^2 [12], the added BA molecule is almost ~10^3 times that of PATP. Even if all PATP molecules participate in the reaction, the amount of product is much less than the amount of reactant BA, which further illustrates the remarkable effect of the electromagnetic field in the cavity. Figure 2E shows the peak strength of random 20 points on the chip at 1075 cm^{-1}, with an RSD (relative standard deviation) of ~8.5%, illustrating that the Raman measurement of the system has a certain repeatability. As shown in Figure S4A, the stretch vibration of the −CH=N− bond at 1654 cm^{-1} certified in the Fourier Transform Infrared (FT-IR) spectrum of NP-PATP-Au TF with decreased BA indicates the triggered Schiff base reaction between PATP and BA [28]. Furthermore, as shown in Figure S4B, the original Raman peak of BA is given to exclude additional interference.

In order to further quantitatively investigate the SERS activity, the SERS spectra of NP-PATP-Au TF with a drop of BA were collected and compared with the Raman spectra of solid PATP (see Figure S5). The sampled volume for the NR spectrum of pure PATP is the product of the laser spot area (diameter is ~1 μm) and the penetration depth of the focused beam (2 μm). Since the density of PATP is 1.18 g cm^{-3}, the number of PATP molecules under laser irradiation is calculated to be 8.9×10^9 (1.5×10^{-14} mol). On the other hand, considering that the density of each PATP molecule at the full coverage limit on Au is 3.3 molecules/nm^2, the number of PATP molecules under laser irradiation is 3.9×10^6. Since the average surface coverage of Au NPs is 2.0/μm^2, the number of Au NPs under laser irradiation is calculated to be 1.6. The number of PATP molecules hidden beneath these Au NPs is about 1.9×10^4, considering that the average diameter of a Au NP is ~42 nm (as depicted in Figure S6). Then, the final enhancement factor (EF) achieved by the attachment of a single Au NP is in the order of 10^5. Considering the weak interaction between -NH_2 and Au NPs, the effect of chemical mechanism on signal enhancement cannot be ignored. Considering that 785 nm photon energy (hν) is 1.58 eV, the body work function (φ) of Au is ~ 5 eV [29,30], and the LUMO orbital energy (E_{LUMO}) of PATP [12] does not meet the resonance conditions of metal–molecular charge transfer ($h\nu \cong \varphi - E_{LUMO}$), Therefore, the contribution of chemical mechanisms to the system is extremely limited. In conclusion, the significant occurrence of the C=N peak can be attributed to two points: (1) The -SH

in PATP in the NP-PATP-TF structure exposes the para-NH_2 by bonding with Au to form a self-assembly layer, making it conducive to chemical reaction. (2) The incident light of 785 nm can produce a very strong local electromagnetic field in the cavity to amplify the weak signal.

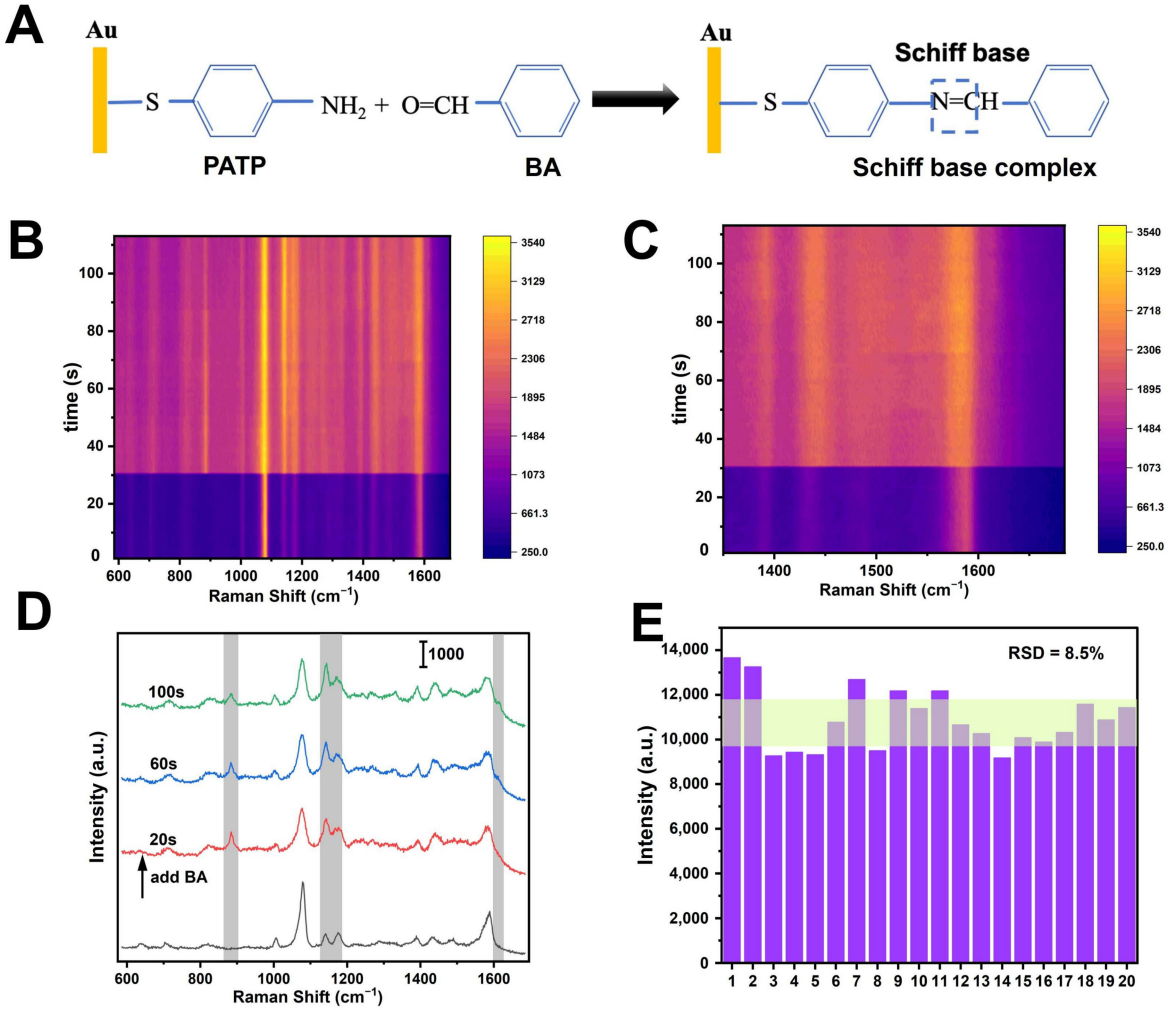

Figure 2. (**A**) A schematic illustration of the strategy used for the detection of BA. (**B**) The time of collection before and after dripping BA (10^{-3} M) on NP-PATP-Au TF platform was dependent on SERS spectrum. (**C**) An enlarged figure obtained by changing the abscissa in (**B**) to 350~1680 cm^{-1}. (**D**) The SERS spectra extracted at different times in Figure (**B**). (**E**) The intensity of characteristic peaks of 1075 cm^{-1} was extracted to make a histogram.

2.2. SERS Sensitivity Test

In addition to effective monitoring, good detection limits are important parameters for evaluating platform functionality. In this test, we first explored the optimal reaction times and temperatures of BA and PATP in ethanol solution. NP-PATP-TF chips were put into 10^{-3} M ethanol solution for a certain time and then rinsed and dried. According to previous experience, the reaction can occur at room temperature, so we set a certain time gradient at room temperature. As shown in Figure 3A, when the captured molecule BA is 10^{-3} M, it can be seen that the reaction reaches equilibrium about 3 min. Therefore, we used this as a reference to set the time parameters in subsequent experiments. It is worth noting that the equilibrium time of chemical reaction would decrease slightly with the decrease in the initial concentration of reactants, so the equilibrium time was slightly weakened under different gradients. Subsequently, the relative peak intensity I_{1620}/I_{1001} was still used as the stability index of the molecular reaction degree, and the corrected product

yield had a good nonlinear relationship with time, which well matched the nonlinear saturation dynamics (as shown in Figure 3B). At the beginning of the reaction, the curve was nearly linear, and the normalized intensity of I_{1620}/I_{1001} tended to be saturated as the reaction progressed more and more fully. The weak peak strength of BA was attributed to a relatively weak molecular adsorption pattern on the surface of Au NPs, such as the π–metal interaction [31]. After exploring suitable reaction conditions, the sensitivity of the system was tested, as shown in Figure 3C. From 10^{-3} M to 10^{-7} M concentrations of BA, the normalized intensity of I_{1620}/I_{1001} gradually weakened to completely disappear, indicating that the detection limit of the system for benzaldehyde is 10^{-6} M. These results provide a basis for the realization of single-molecule-level catalytic process monitoring [32]. Figure 3D shows that the horizontal coordinate of I_{1620}/I_{1001} is the BA concentration after logarithm (base number is 10), and the vertical coordinate is the signal intensity of the characteristic peak. The experimental results are linear and the fitting coefficient $R^2 = 0.997$. This means that the NP-PATP-TF substrate can accurately reflect the amount of reaction products produced by the system through the amplified molecular Raman signal.

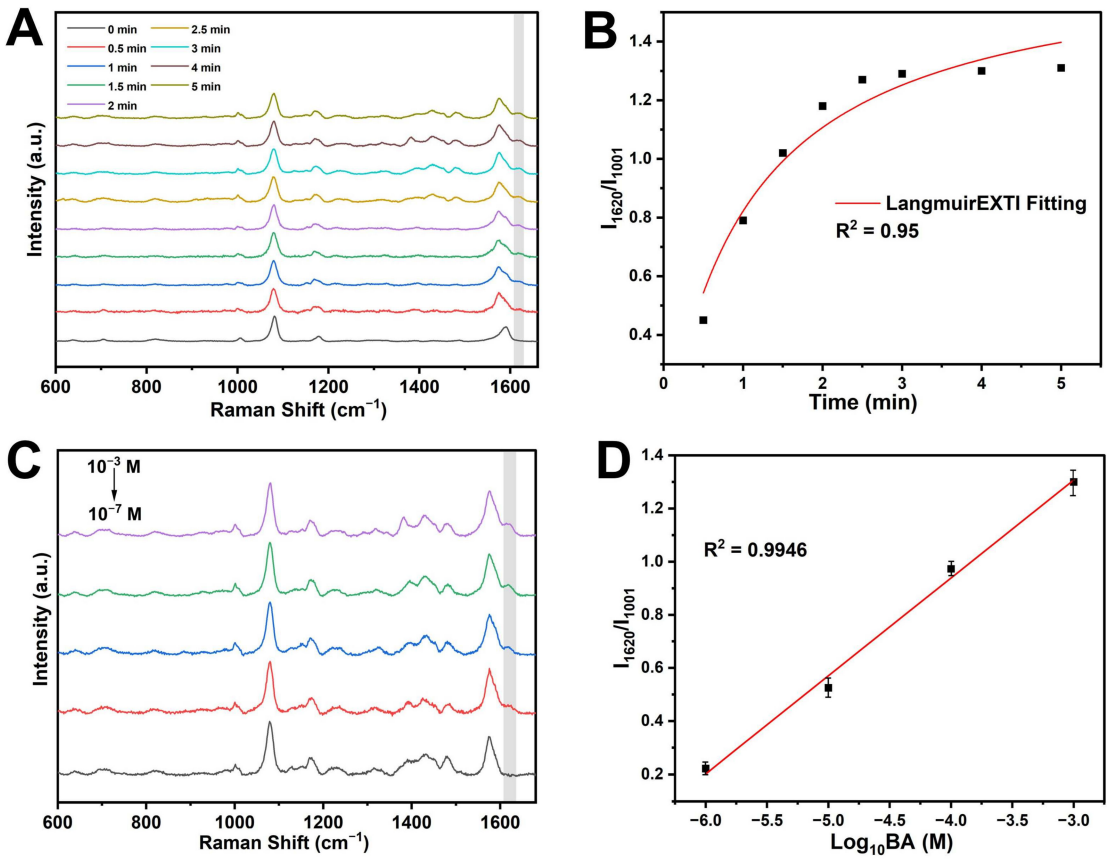

Figure 3. (**A**) In situ SERS monitoring of Schiff base reactions on NP-PATP-TF. The concentration of BA in the ethanol phase is 10^{-3} M. The characteristic peak of C=N in 1620 cm^{-1} is shaded in grey. (**B**) Time-dependent change in the relative peak intensity I_{1620}/I_{1001}. (**C**) Spectral lines of BA concentration from 10^{-7} M to 10^{-3} M in the post-reaction mixture were collected in the standard sample system. The characteristic peak of C=N in 1620 cm^{-1} is shaded in grey. (**D**) Plot of I_{1620}/I_{1001} versus logarithmic BA concentration.

2.3. Anti-Interference and Specificity Test

Finally, the selectivity and anti-interference of the system are evaluated, as shown in Figure 4. We replace benzaldehyde with benzyl alcohol and benzoic acid, which have similar structures but different functional groups. As shown in Figure 4A, when benzyl alcohol and benzoic acid exist alone, no peak of 1620 cm^{-1} appears in the spectrum after

reaction with PATP, as the grey shadow describes, which reflects the selectivity of the system reaction. Figure 4B shows the scatter spacing diagram obtained by correcting the product signal strength according to the benzene ring vibration mode, which further indicates that benzyl alcohol and benzoic acid do not react with PATP. Surprisingly, as shown in Figure 4C, under the interference of benzoic acid and benzyl alcohol, the reaction between BA and PATP is also almost undisturbed, that is, benzoic acid and benzyl alcohol hardly affect the ability of PATP to capture BA. However, under different interference, the degree of condensation reaction decreases slightly (as shown in Figure 4D), which confirms that our SERS method has good anti-interference performance, reflecting the super selectivity and stability of the system.

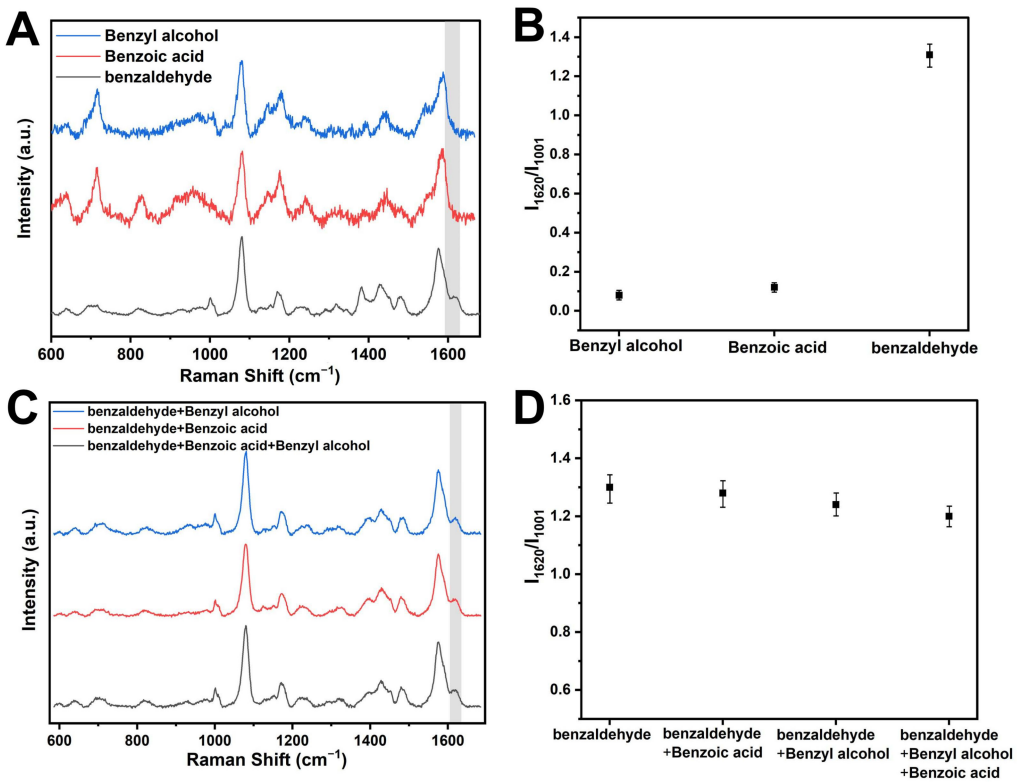

Figure 4. (**A**) The SERS spectrum of the NP-PATP-TF platform selectivity experiment. The characteristic peak of C=N in 1620 cm^{-1} is shaded in grey. (**B**) A scatterplot of product signal strength corrected according to a benzene ring vibration extracted from (**A**). (**C**) An NP-PATP-TF platform anti-interference experiment with the product signal strength corrected according to the benzene ring vibration mode SERS spectrum. The characteristic peak of C=N in 1620 cm^{-1} is shaded in grey. (**D**) A scatterplot of product signal strength corrected according to the benzene ring vibration mode extracted from (**C**).

3. Experimental

3.1. Chemicals Used

Chloroauric acid, trisodium citrate dihydrate, ethanol, p-Aminothiophenol, benzaldehyde, benzoic acid, and benzyl alcohol were purchased from Aladdin (Shanghai, China). An Au thin film on silicon was purchased from Nashuo electronic materials store (Haerbin, China). All chemicals were used without further purification, unless otherwise specified. The entire experiment was conducted at room temperature, with deionized water (DI) used for preparing the relevant solutions.

3.2. Synthesis of Au NPs

Au NPs were prepared by the classical hot reduction method of sodium citrate solution [33–35]. First, we dissolved 0.097 g of sodium citrate into 150 mL of deionized water

and heated it in a water bath for 15 min, stirring continuously during the process. Then, 1 mL of 0.98 wt% $HAuCl_4 \cdot 3H_2O$ solution was added and stirred for 10 min after boiling, and then it was cooled down to 90 °C. A total of 0.176 g of sodium citrate was dissolved in 10 mL deionized water to make a 60 mM sodium citrate solution. Then, 2 mL of sodium citrate solution was added to a Au NP solution, and we kept heating at 90 °C for 2 min, then added 1 mL of 0.98 wt% $HAuCl_4 \cdot 3H_2O$ solution, continued heating for 30 min, and repeated this step three times. The obtained Au solution was then removed and cooled to room temperature (RT).

3.3. Preparation of NP-PATP-TF Structure

A fully saturated self-assembled monolayer PATP (SAM-PATP) [36] was formed on the Au thin film by dipping a gold-plated silicon wafer into an ethanol solution of 4-aminobenzene mercaptan at 0.001 M for ~30 min. The sample was then rinsed with ethanol to remove excess PATP from the surface, and the SAM-Au film was then obtained. Then, the Au solution after cleaning was redispersed with a mixture of water and ethanol at 1:1, and the surface of SAM-Au was coated with a differential spin and then rinsed and dried at room temperature to obtain NP-PATP-TF, as shown in Scheme 1.

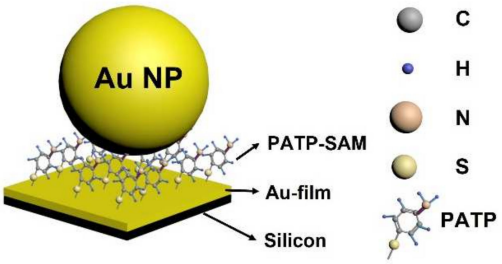

Scheme 1. The structure of the NP-PATP-TF platform.

3.4. Raman Performance Testing

The SERS performance of a pure NP-PATP-TF chip was tested to ensure it exhibited good uniformity and reproducibility. Then, the BA solution prepared with ethanol was added to the chip surface, and the in situ Raman test was carried out immediately. SERS measurements were performed using laser micro-confocal Raman spectroscopy (RENISHAW inVia, Beijing, China) upon 785 nm excitation. A 50× objective lens was utilized to focus the excitation light on the SERS substrate for the collection of Raman signals.

4. Conclusions

In summary, by utilizing the NP-PATP-TF platform and taking advantage of the exposure of $-NH_2$ groups in the nanocavity and the localized strong electromagnetic field, the occurrence of the Schiff base reaction can be rapidly monitored within two minutes, achieving quick monitoring on a simple and easy-to-use preparation platform. Due to the strong localized electromagnetic field generated in the cavity formed by the platform, the Raman signals are significantly enhanced, allowing for the detection of BA at sub-ppb levels. And the platform also exhibits specificity and anti-interference, attributed to the specific reaction between the -CHO group of BA and the $-NH_2$ group of PATP. Compared with traditional sensing methods, the NP-PATP-TF system can not only realize in situ monitoring but also has accuracy, specificity and simplicity of operation. It achieves a balance between low cost and high performance, offering considerable potential for applications in revealing the mechanism of plasmon catalysis.

Supplementary Materials: The following supporting information can be downloaded at: https://www.mdpi.com/article/10.3390/catal14110803/s1, Figures S1–S6: SEM image of NP-PATP-TF chip cross section and elemental mapping image of Au, Extended SERS spectrum of PATP on the NP-PATP- TF structure, High-resolution XPS spectra of Au 4f of Au film, Fourier Transform infrared spectra of NP-PATP-Au TF and Normal Raman spectra of benzaldehyde, Normal Raman spectra of

PATP solid powder, Dynamic light scattering results of Au NPs sol; Table S1: Mode assignment of the Raman peaks for PATP.

Author Contributions: Conceptualization, B.C.; Methodology, B.C. and S.M.; Software, B.C.; Validation, B.C.; Formal analysis, B.C.; Investigation, B.C. and S.M.; Data curation, B.C.; Writing—original draft, B.C.; Writing—review & editing, C.W.; Visualization, S.M.; Resources, D.L. and Q.D.; Supervision, C.W.; Project administration, C.W.; Funding acquisition, Q.D. and C.W. All authors have read and agreed to the published version of the manuscript.

Funding: This research was funded by the National Natural Science Foundation of China (Grant No. 12104023), Beijing Natural Science Foundation (Grant No. L248027, Z210006 and L245019), Ningbo Institute of Life and Health Industry Program (Grant No. 2022YJY1101).

Data Availability Statement: Data are contained within the article and Supplementary Materials.

Conflicts of Interest: The authors declare no conflict of interest.

References

1. Kalkan, A.K. Single Molecule Detection Surface-Enhanced Raman Scattering Substrates by Electroless Synthesis of Ag Nanoparticles on Nanostructured Silicon Films. *ECS Trans.* **2007**, *3*, 9. [CrossRef]
2. Sharma, B.; Frontiera, R.R.; Henry, A.-I.; Ringe, E.; Van Duyne, R.P. SERS: Materials, Applications, and the Future. *Mater. Today* **2012**, *15*, 16–25. [CrossRef]
3. Yang, N.; You, T.; Gao, Y.; Lu, S.; Yin, P. One-Step Preparation Method of Flexible Metafilms on the Water–Oil Interface: Self-Assembly Surface Plasmon Structures for Surface-Enhanced Raman Scattering Detection. *Langmuir* **2019**, *35*, 4626–4633. [CrossRef] [PubMed]
4. Liu, Y.; Ma, H.; Han, X.X.; Zhao, B. Metal–Semiconductor Heterostructures for Surface-Enhanced Raman Scattering: Synergistic Contribution of Plasmons and Charge Transfer. *Mater. Horiz.* **2021**, *8*, 370–382. [CrossRef] [PubMed]
5. Liu, Y.; Zhou, J.; Wang, B.; Jiang, T.; Ho, H.-P.; Petti, L.; Mormile, P. Au@Ag Core–Shell Nanocubes: Epitaxial Growth Synthesis and Surface-Enhanced Raman Scattering Performance. *Phys. Chem. Chem. Phys.* **2015**, *17*, 6819–6826. [CrossRef]
6. Jin, X.; Zhu, Q.; Feng, L.; Li, X.; Zhu, H.; Miao, H.; Zeng, Z.; Wang, Y.; Li, Y.; Wang, L.; et al. Light-Trapping SERS Substrate with Regular Bioinspired Arrays for Detecting Trace Dyes. *ACS Appl. Mater. Interfaces* **2021**, *13*, 11535–11542. [CrossRef]
7. Wang, X.; Guo, L. SERS Activity of Semiconductors: Crystalline and Amorphous Nanomaterials. *Angew. Chem. Int. Ed.* **2020**, *59*, 4231–4239. [CrossRef]
8. Yang, J.; Xu, J.; Bian, X.; Pu, Y.; Chiu, K.L.; Miao, D.; Jiang, S. Flexible and Reusable SERS Substrate for Rapid Conformal Detection of Residue on Irregular Surface. *Cellulose* **2021**, *28*, 921–936. [CrossRef]
9. Lee, S. Nanoparticle-on-Mirror Cavity: A Historical View across Nanophotonics and Nanochemistry. *J. Korean Phys. Soc.* **2022**, *81*, 502–509. [CrossRef]
10. Huh, J.-H.; Lee, J.; Lee, S. Comparative Study of Plasmonic Resonances between the Roundest and Randomly Faceted Au Nanoparticles-on-Mirror Cavities. *ACS Photonics* **2018**, *5*, 413–421. [CrossRef]
11. Kim, K.; Yoon, J.K. Raman Scattering of 4-Aminobenzenethiol Sandwiched between Ag/Au Nanoparticle and Macroscopically Smooth Au Substrate. *J. Phys. Chem. B* **2005**, *109*, 20731–20736. [CrossRef]
12. Park, W.-H.; Kim, Z.H. Charge Transfer Enhancement in the SERS of a Single Molecule. *Nano Lett.* **2010**, *10*, 4040–4048. [CrossRef] [PubMed]
13. Chikkaraddy, R.; de Nijs, B.; Benz, F.; Barrow, S.J.; Scherman, O.A.; Rosta, E.; Demetriadou, A.; Fox, P.; Hess, O.; Baumberg, J.J. Single-Molecule Strong Coupling at Room Temperature in Plasmonic Nanocavities. *Nature* **2016**, *535*, 127–130. [CrossRef] [PubMed]
14. Baumberg, J.J.; Aizpurua, J.; Mikkelsen, M.H.; Smith, D.R. Extreme Nanophotonics from Ultrathin Metallic Gaps. *Nat. Mater.* **2019**, *18*, 668–678. [CrossRef] [PubMed]
15. Wright, D.; Lin, Q.; Berta, D.; Földes, T.; Wagner, A.; Griffiths, J.; Readman, C.; Rosta, E.; Reisner, E.; Baumberg, J.J. Mechanistic Study of an Immobilized Molecular Electrocatalyst by in Situ Gap-Plasmon-Assisted Spectro-Electrochemistry. *Nat. Catal.* **2021**, *4*, 157–163. [CrossRef]
16. Di Martino, G.; Demetriadou, A.; Li, W.; Kos, D.; Zhu, B.; Wang, X.; de Nijs, B.; Wang, H.; MacManus-Driscoll, J.; Baumberg, J.J. Real-Time in Situ Optical Tracking of Oxygen Vacancy Migration in Memristors. *Nat. Electron.* **2020**, *3*, 687–693. [CrossRef]
17. Xia, Z.; Li, D.; Deng, W. Identification and Detection of Volatile Aldehydes as Lung Cancer Biomarkers by Vapor Generation Combined with Paper-Based Thin-Film Microextraction. *Anal. Chem.* **2021**, *93*, 4924–4931. [CrossRef]
18. Nguyen, L.B.T.; Leong, Y.X.; Koh, C.S.L.; Leong, S.X.; Boong, S.K.; Sim, H.Y.F.; Phan-Quang, G.C.; Phang, I.Y.; Ling, X.Y. Inducing Ring Complexation for Efficient Capture and Detection of Small Gaseous Molecules Using SERS for Environmental Surveillance. *Angew. Chem. Int. Ed.* **2022**, *61*, e202207447. [CrossRef]
19. Huang, Y.; Xie, T.; Zou, K.; Gu, Y.; Yang, G.; Zhang, F.; Qu, L.-L.; Yang, S. Ultrasensitive SERS Detection of Exhaled Biomarkers of Lung Cancer Using a Multifunctional Solid Phase Extraction Membrane. *Nanoscale* **2021**, *13*, 13344–13352. [CrossRef]

20. Yang, K.; Zong, S.; Zhang, Y.; Qian, Z.; Liu, Y.; Zhu, K.; Li, L.; Li, N.; Wang, Z.; Cui, Y. Array-Assisted SERS Microfluidic Chips for Highly Sensitive and Multiplex Gas Sensing. *ACS Appl. Mater. Interfaces* **2020**, *12*, 1395–1403. [CrossRef]
21. Chen, Z.; Li, G.; Zhang, Z. Miniaturized Array Gas Membrane Separation Strategy for Rapid Analysis of Complex Samples by Surface-Enhanced Raman Scattering. *Anal. Chim. Acta* **2019**, *1065*, 29–39. [CrossRef] [PubMed]
22. Huang, L.; Zhu, Y.; Xu, C.; Cai, Y.; Yi, Y.; Li, K.; Ren, X.; Jiang, D.; Ge, Y.; Liu, X.; et al. Noninvasive Diagnosis of Gastric Cancer Based on Breath Analysis with a Tubular Surface-Enhanced Raman Scattering Sensor. *ACS Sens.* **2022**, *7*, 1439–1450. [CrossRef] [PubMed]
23. Huh, H.; Trinh, H.D.; Lee, D.; Yoon, S. How Does a Plasmon-Induced Hot Charge Carrier Break a C–C Bond? *ACS Appl. Mater. Interfaces* **2019**, *11*, 24715–24724. [CrossRef]
24. Tagliabue, G.; DuChene, J.S.; Abdellah, M.; Habib, A.; Gosztola, D.J.; Hattori, Y.; Cheng, W.-H.; Zheng, K.; Canton, S.E.; Sundararaman, R.; et al. Ultrafast Hot-Hole Injection Modifies Hot-Electron Dynamics in Au/p-GaN Heterostructures. *Nat. Mater.* **2020**, *19*, 1312–1318. [CrossRef]
25. Baumberg, J.J. Picocavities: A Primer. *Nano Lett.* **2022**, *22*, 5859–5865. [CrossRef] [PubMed]
26. Varnholt, B.; Oulevey, P.; Luber, S.; Kumara, C.; Dass, A.; Bürgi, T. Structural Information on the Au–S Interface of Thiolate-Protected Gold Clusters: A Raman Spectroscopy Study. *J. Phys. Chem. C* **2014**, *118*, 9604–9611. [CrossRef]
27. Qiao, X.; Su, B.; Liu, C.; Song, Q.; Luo, D.; Mo, G.; Wang, T. Selective Surface Enhanced Raman Scattering for Quantitative Detection of Lung Cancer Biomarkers in Superparticle@MOF Structure. *Adv. Mater.* **2018**, *30*, 1702275. [CrossRef]
28. Shao, G.; Shen, X.; Huang, X. Multilevel Structural Design and Heterointerface Engineering of a Host–Guest Binary Aerogel toward Multifunctional Broadband Microwave Absorption. *ACS Mater. Lett.* **2022**, *4*, 1787–1797. [CrossRef]
29. Handoko, A.D.; Steinmann, S.N.; Seh, Z.W. Theory-Guided Materials Design: Two-Dimensional MXenes in Electro- and Photocatalysis. *Nanoscale Horiz.* **2019**, *4*, 809–827. [CrossRef]
30. Wang, X.; Tian, X.; Sun, Y.; Zhu, J.; Li, F.; Mu, H.; Zhao, J. Enhanced Schottky Effect of a 2D–2D CoP/g-C3N4 Interface for Boosting Photocatalytic H2 Evolution. *Nanoscale* **2018**, *10*, 12315–12321. [CrossRef]
31. Wang, H.; Wei, Y.; Wang, L.; Qu, C.; Liu, H.; He, S. Portable SERS Sensing of Volatile Aldehydes in Alcohols by Aldol Condensation Reaction on Liquid Interfacial Plasmonic Arrays. *Chem. Commun.* **2023**, *59*, 12342–12345. [CrossRef] [PubMed]
32. Choi, H.-K.; Park, W.-H.; Park, C.-G.; Shin, H.-H.; Lee, K.S.; Kim, Z.H. Metal-Catalyzed Chemical Reaction of Single Molecules Directly Probed by Vibrational Spectroscopy. *J. Am. Chem. Soc.* **2016**, *138*, 4673–4684. [CrossRef] [PubMed]
33. Turkevich, J.; Stevenson, P.C.; Hillier, J. A Study of the Nucleation and Growth Processes in the Synthesis of Colloidal Gold. *Discuss. Faraday Soc.* **1951**, *11*, 55–75. [CrossRef]
34. Dou, Y.; Guo, Y.; Li, X.; Li, X.; Wang, S.; Wang, L.; Lv, G.; Zhang, X.; Wang, H.; Gong, X.; et al. Size-Tuning Ionization To Optimize Gold Nanoparticles for Simultaneous Enhanced CT Imaging and Radiotherapy. *ACS Nano* **2016**, *10*, 2536–2548. [CrossRef]
35. Tran, M.; DePenning, R.; Turner, M.; Padalkar, S. Effect of Citrate Ratio and Temperature on Gold Nanoparticle Size and Morphology. *Mater. Res. Express* **2016**, *3*, 105027. [CrossRef]
36. Ye, J.; Hutchison, J.A.; Uji-i, H.; Hofkens, J.; Lagae, L.; Maes, G.; Borghs, G.; Dorpe, P.V. Excitation Wavelength Dependent Surface Enhanced Raman Scattering of 4-Aminothiophenol on Gold Nanorings. *Nanoscale* **2012**, *4*, 1606–1611. [CrossRef]

Disclaimer/Publisher's Note: The statements, opinions and data contained in all publications are solely those of the individual author(s) and contributor(s) and not of MDPI and/or the editor(s). MDPI and/or the editor(s) disclaim responsibility for any injury to people or property resulting from any ideas, methods, instructions or products referred to in the content.